Surface & Coatings Technology 434 (2022) 128178

Contents lists available at ScienceDirect

Surface & Coatings Technology

journal homepage: www.elsevier.com/locate/surfcoat

Influence of Si on the oxidation behavior of TM-Si-$B_{2\pm z}$ coatings (TM = Ti, Cr, Hf, Ta, W)

T. Glechner [a,*], H.G. Oemer [a], T. Wojcik [a], M. Weiss [b], A. Limbeck [b], J. Ramm [c], P. Polcik [d], H. Riedl [a,e]

[a] Christian Doppler Laboratory for Surface Engineering of High-Performance Components, TU Wien, Austria
[b] Institute of Chemical Technologies and Analytics, TU Wien, A-1060 Wien, Austria
[c] Oerlikon Balzers, Oerlikon Surface Solutions AG, FL-9496 Balzers, Liechtenstein
[d] Plansee Composite Materials GmbH, D-86983 Lechbruck am See, Germany
[e] Institute of Materials Science and Technology, TU Wien, A-1060 Wien, Austria

ARTICLE INFO

Keywords:
Diborides
Oxidation resistance
Si alloying
Scale formation

ABSTRACT

The concept of Si alloyed transition metal (TM) diborides – well explored for bulk ceramics – is studied for five different physical vapor deposited TM-Si-$B_{2\pm z}$ (TM = Ti, Cr, Hf, Ta, W) coatings, focusing on the oxidation behavior up to 1200 °C. In their as deposited state, all coatings exhibit single phased AlB_2 prototype structures, whereby the addition of Si results in dense, refined morphologies with no additional phases visible in the X-ray diffractograms. With already low amounts of Si, the slope of the mass increase during dynamic oxidation flattens, especially for Ti-Si-$B_{2\pm z}$, Cr-Si-$B_{2\pm z}$, and Hf-Si-$B_{2\pm z}$. Above distinct Si contents, the formation of a steady state region exhibiting no further mass increase is promoted (starting at around 1000 to 1100 °C). Best results are obtained for $Hf_{0.21}Si_{0.18}B_{0.61}$ and $Cr_{0.26}Si_{0.16}B_{0.58}$ (both around 2.4 μm thick in the as deposited sate), revealing drastically retarded oxidation kinetics forming 400 nm thin oxide scales after 3 h at 1200 °C in ambient air (significantly lower compared to bulk ceramics). This highly protective oxidation mechanism is attributed to the formation of an amorphous Si rich oxide scale. The Si content needed to form these oxide scales largely differs between the TM-Si-$B_{2\pm z}$ coatings investigated, also diversifying the prevalent oxidation mechanism, especially for Cr-Si-$B_{2\pm z}$.

1. Introduction

Transition metal (TM) boride based thin films are an emerging class of coating materials initiating an extremely broad field of new applications [1–6]. The origins of the diverse properties are the specific bonding nature of boron – forming different versions of covalently bonded sheets within metal layers [7] – as well as the broad stoichiometric and crystallographic variation ranging from i.e. TMB_2 up to TMB_{66} [8–10]. Under extremely harsh conditions (high temperatures and aggressive atmospheres), these ultra-high temperature ceramics are well-known for their refractory character involving melting temperatures above 3000 °C, a wide phase stability, high thermal conductivity [11], as well as strong thermo-shock resistance [12,13]. Increasing interest in a sustainable usage of materials as well as the longevity of high-performance components – e.g. machine elements in aero engines – suggest TM boride based materials as a new class of protective thin films [14,15]. However, in the field of transition metal diboride based coatings, there are two stumbling blocks being part of diverse scientific studies: *(i)* the poor fracture tolerance [16,17] and *(ii)* the limited oxidation resistance [14,18].

These issues are of course also known for diboride bulk ceramics, where diverse concepts have been elaborated [12,19]. As this study focuses on the oxidation resistance of transition metal diboride (TMB) based coatings, it is worth revisiting different bulk alloying concepts proving an enhanced oxidation resistance, especially in the temperature range above 1000 °C. When oxidizing diboride based bulk ceramics typically an oxide scale with a glassy top B_2O_3 (boria) layer is formed, as reported for i.e. TiB_2, ZrB_2, and HfB_2 [12,20,21]. In detail, three different regimes can be distinguished: *(i)* a low temperature regime typically below 900 to 1000 °C obtaining a crystalline metal oxide layer with a more or less dense boria layer on top, *(ii)* a second regime up to 1600 to 1800 °C with an initial evaporation of the top B_2O_3, and *(iii)* the

* Corresponding author.
E-mail address: thomas.glechner@tuwien.ac.at (T. Glechner).

https://doi.org/10.1016/j.surfcoat.2022.128178
Received 24 December 2021; Received in revised form 24 January 2022; Accepted 27 January 2022
Available online 3 February 2022

last regime above 1800 °C being dominated by the volatile evaporation of boria next to porous metal oxides [12,20]. However, also environmental conditions such as atmospheric humidity or flow conditions can influence the oxide scale formation of TM borides. Here, the presence of water vapor is reported to expedite the formation of volatile boric acid (HBO_2) promoting the volatility of boria, and hence decreasing the oxidation resistance [22,23]. Nevertheless, a recent study confirmed a similar oxidation behavior for a $HfB_{2.3}$ coating compared to its bulk ceramic counterpart forming also a layered, but dense scale at 900 °C, pursuing a parabolic rate law with the rate constant k_p of $1.39 \cdot 10^{-9}$ $kg^2m^{-4}\ s^{-1}$ [24]. To sustain long term oxidation at elevated temperatures (>1000 °C), only alumina and silica based oxide scales provide sufficiently low parabolic rate constants – proposed to be in the range of 10^{-10} $kg^2m^{-4}\ s^{-1}$ at 1100 °C [25,26]. For bulk TM diborides (especially ZrB_2 and HfB_2) the addition of 20 vol% SiC (or other Si containing phases like metal-silicides) was found to be very effective in decreasing oxide scale growth rates [12,27] and opened a wide field of ongoing research [28]. These additional Si containing phases are predominant in the oxide scale formation, leading to a highly protective (withstanding temperatures above 1200 °C), glassy like borosilicate layer, instead of a less protective B_2O_3 – similar to approaches used for refractory metal silicides [29–32]. For enhancing the oxidation resistance of transition metal diboride based thin films, only limited alloying strategies are known. First, the influence of Si on TM boride based coatings was investigated for TiB_2 up to 900 °C [33] as well as ZrB_2 above 1000 °C [34,35]. Alloying with Al showed some improvements for TiB_2 coatings [14] (similar to enhancements with Ta for WB_2 [18]), but being behind its nitride based counterpart, Ti-Al-N [14,18]. On the other hand, the MAB coating, MoAlB, showed a quite retarded oxide growth at 1200 °C, but only proven for 30 min [36]. Here, we want to emphasize, that this is just an incomplete list mentioning promising approaches. Nonetheless, the oxidation resistance of diboride based protective thin films presents still a relatively uncharted territory, rising interesting opportunities in relation to diboride bulk ceramics.

Therefore, in this study we want to elaborate the Si alloying route for a broad set of transition metal diboride based coating materials (TM-Si-$B_{2\pm z}$, TM = Ti, Cr, Hf, Ta, and W) pursuing different aspects, namely: *(i)* influence of the limited kinetics during physical vapor deposition (PVD) to form TM-Si-$B_{2\pm z}$ solid solutions, *(ii)* ratio between Si and B to promote a borosilicate or silica enriched scaling, and *(iii)* effectiveness of this alloying approach with respect to the different transition metals.

2. Methods

All TM-Si-$B_{2\pm z}$ based thin films were deposited using an in-house built magnetron sputter deposition system [37]. To gain a broader view on the Si alloying route, we chose five different TM diborides from group IV to VI, in detail TiB_2, CrB_2, HfB_2, TaB_2, and W_2B_5 (all 3-in. sized targets have been provided by Plansee Composite Materials GmbH, at least 99.6% purity). To add silicon, we used the simple but very effective approach of putting single crystalline Si plates (100 oriented, n-phosphorus type, 7x7x0.38 mm^3, CrysTec GmbH) onto the sputter racetrack. The sputter racetrack covered an averaged area of about 15 cm^2 of the total target surface (45 cm^2). By varying the number of pieces (2 to 8 platelets), we modified the Si content within the TM-Si-$B_{2\pm z}$ coatings. The targets were operated in DC mode with a current of 0.5 A (0.4 A for CrB_2) in pure argon atmosphere (99.999% purity), at a working pressure of 0.56 Pa. The thin films were deposited on polycrystalline Al_2O_3 (20x7x0.38 mm^3, used for oxidation in the TG system), single crystalline Si (20x7x0.38 mm^3, used for micrographs in the as deposited state) and sapphire (10x10x0.53 mm^3, used for nanoindentation and oxidation in box furnace) substrates at a target to substrate distance of 90 mm. A substrate temperature of 550 °C as well as a bias potential of −40 V was used for all depositions.

For stoichiometry determination, samples were analyzed by liquid Inductively Coupled Plasma Optical Emission Spectroscopy (ICP-OES) after acid digestion. To exclude silicon contamination from the substrates, only samples on Al_2O_3 wafers were investigated. The used method was validated in [38]. All chemicals were of the highest purity available, ultrapure water with a resistivity of 18.2 MΩ was obtained by a Barnstead EASYPURE II water system (Thermo Fisher Scientific, USA), single element ICP standards and concentrated acids were purchased from Merck (Germany). Samples were broken into 5 × 5 mm pieces and digested in triplicates with a mixture of 0.5 mL HNO_3 and 0.5 ml HF in falcon tubes, by heating to 80 °C for 10 min. The samples were afterwards diluted to a volume of 20 ml with H_2O and europium was as internal added, to yield a final concentration of 1 μg/g europium. Samples were measured with an iCAP 6500 RAD (Thermo Fisher, USA), with an ASX-520 autosampler (CETAC Technologies, USA) using a HF resistant sample introduction kit, consisting of a Miramist nebulizer (Burger Research, USA), an alumina injector tube and a PTFE spray chamber. Background corrected emission signals were quantified using matrix adjusted external calibration standards.

The mechanical properties were assessed by Nanoindentation using an Ultra Micro Indentation System (UMIS) equipped with a Berkovich diamond tip (all measurements done on sapphire substrates). For every sample, 30 idents with different applied loads (3 to 45 mN) were performed and their load-displacement curves were analyzed after Oliver and Pharr [27]. Poisson ratios for calculating the Young's modulus were taken from Ref. [16].

To study the oxidation behavior of the deposited coatings we used a Thermo-Gravimetric Analysis (TGA) system, which was equipped with a Rhodium oven (Netzsch STA 449 F1). The TGA system has a resolution of 0.1 μg, obtaining a limit of about 10 μg to detected significant effects. The polycrystalline Al_2O_3 substrates were weighed before and after the deposition to determine the weight of the coatings and subsequently put into a customized crucible. Dynamic oxidation treatments (steady temperature rise between RT and 1400 °C) were carried out under a flowing stream of synthetic air (50 ml/min) and helium (20 ml/min), which is necessary to protect the scales (heating rate of 10 K/min). For isothermal oxidation synthetic air was only flowing through the furnace during the isothermal step. In addition, a baseline measurement with empty crucibles was carried out for each run. Furthermore, the dynamic oxidation of an uncoated Al_2O_3 substrate showed no significant mass change over temperature, as shown in Fig. A1 (see Appendix). Hence a possible contribution of the Al_2O_3 substrate to the measured mass change of the coatings during oxidation can be excluded. In addition, oxidation treatments in ambient air at 1200 °C have been carried out in a standardized chamber box furnace, placing the coated substrates on fireclay tile.

X-ray diffraction (XRD) analysis was done in Bragg Brentano configuration, using a Panalytical Empyrean diffractometer equipped with a Cu-K_α radiation source (wavelength λ = 1.5418 Å). The morphology and oxide scale thickness were studied using a scanning electron microscope (SEM, FEI Quanta 250 FEGSEM operated at 5 kV). Furthermore, for more detailed investigation of the oxidized samples transmission electron microscopy (TEM, FEI TECNAI F20, equipped with a field emission gun and operated at an accelerating voltage of 200 kV) was conducted. Bright field (BF) dark field (DF) imaging and selected area electron diffraction (SAED) reveals the microstructure, crystal structures and texture, whereas high angle annular dark field (HAADF, mass contrast) images and energy dispersive x-ray spectroscopy (EDX) line scans in scanning TEM (STEM) mode provide information about the chemical composition. Furthermore, electron energy-loss spectroscopy (EELS) was carried out to determine the composition of the oxide scale. An entrance aperture with 2 mm was used to record the spectrum from 50 to 1050 eV and the Si L (99 eV), B K (188 eV) and O k (532 eV) edges were used for quantification.

3. Results

The chemical compositions for all coatings obtained by ICP-OES are

shown in Fig. 1a, indicating the B/TM ratio against the silicon content (the numbers next to the symbols denote to the quantity of Si platelets used). In general, the stoichiometry of the binary thin films varied between metal deficient TMB_{2+z} (for $TiB_{2.72}$, $CrB_{2.27}$, and $HfB_{2.36}$) as well as boron deficient coatings, meaning TMB_{2-z} ($TaB_{1.53}$ and $WB_{1.88}$). For $WB_{2\pm z}$ we obtained a stoichiometry close to the 2 to 1 stoichiometry ($WB_{1.88}$) despite using a target with a W_2B_5 stoichiometry. For $TiB_{2.72}$ one reason of the boron over-stoichiometry can be attributed to scattering effects of Ti and B with the working gas, according to Neidhardt et al. [39]. While this might be also applicable for $CrB_{2.27}$ (similar mass as Ti), it becomes difficult to explain why $TaB_{1.53}$ and $WB_{1.88}$ are sub-stoichiometric especially compared to $HfB_{2.36}$, having similar atomic masses. A possible explanation might be the different tendencies to form structural defects. According to density functional theory calculations, carried out by Moraes et al., are α-structured Ta and W diboride strongly stabilized by boron and metal vacancies, whereas Ti and Hf diboride prefer perfect structures. CrB_2 is located in between obtaining small energy gains while introducing boron vacancies compared to slight losses removing metal atoms. Considering these stabilization criteria for the growth of α-structured diborides – obtaining extreme kinetic conditions during PVD – the film stoichiometry is not only influenced by scattering effects, but also by the prevalent thermodynamic driving forces. This is also in good agreement to other studies obtaining similar tendencies, e.g. magnetron sputtered TiB_{2+z} and ZrB_{2+z} coatings are over stoichiometric [14,40] whereas TaB_{2-z} and WB_{2-z} are again under stoichiometric [18]. However, by strongly influencing the plasma conditions through ionization, the thermodynamic dominance might change [41].

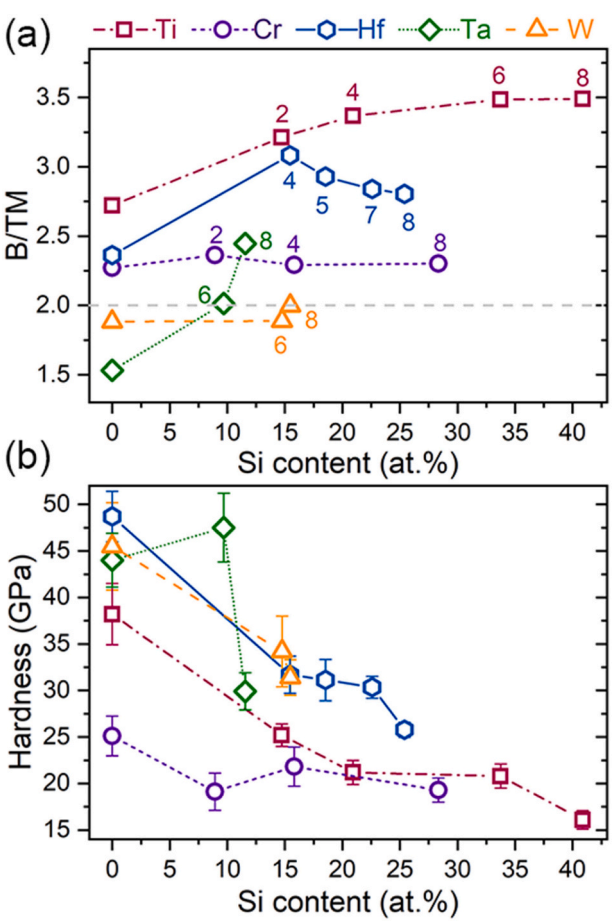

Fig. 1. (a) Chemical composition of all as deposited coatings determined by ICP-OES. The grey dashed line represents the B/TM ratio of a stoichiometric TMB_2 coating material. Numbers denote the quantity of Si platelets used to obtain the composition. (b) Hardness determined using nanoindentation for all coatings in the as deposited state.

Nevertheless, by adding Si in the sputter process the superposition between scattering effects and defect formation gets more complex. The silicon content for each system increases more or less linearly with an increasing number of Si platelets placed on the racetrack, see Fig. 1a. Nevertheless, the highest Si content was achieved for TiB_{2+z} (Si = 41 at. % using 8 platelets) as well as the lowest for TaB_{2-z} (Si = 12 at.% using 8 platelets). Furthermore, the B/TM ratio stayed relatively constant for Cr and W based coatings, suggesting that Si is either randomly incorporated at TM and B sites, or predominantly present as a separate phase at the grain boundaries. In contrast, for Ti and especially Ta based coatings the B/TM ratio increased steadily, which may indicate that Si predominantly occupies metal sites. For Hf based coatings no clear trend is visible, as the B/TM ratio is highest for the lowest amount of Si platelets. In summary, the authors have to state, that the observed stoichiometry evolutions are not fully clear and open questions still remain. Hence, further studies have to be carried out to fully reveal the mechanisms causing the different diboride stoichiometries. Here, the comparison of the coating but also target compositions using complementary analysis techniques would be essential, as well as a systematic screening of the deposition conditions (similar to the study by Neidhardt et al. [39]).

In Fig. 1b the influence of Si on the mechanical properties (in detail hardness) of all TM-Si-$B_{2\pm z}$ is summarized. The binary coatings exhibit very high hardness values of 38.2 ± 3.3 GPa for $TiB_{2.72}$, 25.1 ± 2.1 GPa for $CrB_{2.27}$, 48.7 ± 2.7 GPa for $HfB_{2.36}$, 44 ± 2.9 GPa for $TaB_{1.53}$, and 45.5 ± 2.7 GPa for $WB_{1.88}$. All Si alloyed thin films show a decreased hardness, except $Ta_{0.30}Si_{0.10}B_{0.60}$ exhibiting 47.5 ± 3.7 GPa. At around 15 at. % Si the hardness is in the range of 25, 22, 32, 30, and 31 GPa for Ti, Cr, Hf, Ta and W based coatings, respectively. The hardness and Young's modulus of the coatings being investigated in more detail are: H = 16.5 ± 0.9 GPa and E = 291 ± 10 GPa for $Ti_{0.13}Si_{0.41}B_{0.46}$, H = 22 ± 2.1 GPa and E = 410 ± 31 GPa for $Cr_{0.26}Si_{0.16}B_{0.58}$, H = 32 ± 2.2 GPa and E = 468 ± 34 GPa for $Hf_{0.21}Si_{0.18}B_{0.61}$, H = 30 ± 2.0 GPa and E = 419 ± 30 GPa for $Ta_{0.26}Si_{0.12}B_{0.62}$, as well as H = 31.4 ± 1.9 and GPa E = 465 ± 52 GPa for $W_{0.28}Si_{0.16}B_{0.56}$.

In Fig. 2, the mass change in relation to the temperature during dynamic oxidation is plotted in percent, with respect to the as deposited coating mass. The dashed lines correspond to the binary TM-$B_{2\pm z}$ coatings, while the solid lines indicate the Si alloyed coatings investigated in more detail. In addition, the dotted and dash-dotted lines represent all further TM-Si-$B_{2\pm z}$ coatings. In general, the mass signals are constant up to a certain temperature indicating no oxide scale formation – referred to as oxidation onset temperature – followed by an increase in mass, due to a progressing oxidation. The oxidation onset temperature is the lowest for $TiB_{2.72}$ (490 °C) and $WB_{1.88}$ (500 °C), followed by $CrB_{2.27}$ (610 °C) and $TaB_{1.53}$ (620 °C), and highest for $HfB_{2.36}$ (800 °C), respectively. Above this onset temperature the mass increases till the coating is fully oxidized and then subsequently decreases, which is assumed to be due to volatilization of B_2O_3 – typically above 1100 °C [12]. For transition metals such as tungsten, also the formation of volatile oxides like WO_3 needs to be considered, causing a further mass decrease even below the initial weight of the coatings [42]. The mass increase of the binary coatings can be steady as for $TaB_{1.53}$ (see Fig. 2d) or more complex obtaining a stepwise oxide scale formation as for $CrB_{2.27}$ (see Fig. 2b). With already low amounts of additional Si, the slope of the mass increase flattens, especially for Ti-Si-$B_{2\pm z}$, Cr-Si-$B_{2\pm z}$, and Hf-Si-$B_{2\pm z}$. For even higher Si contents a plateau of a steady mass signal is achieved (above 1000 to 1100 °C) – suggesting a strongly delayed oxidation process – having a protective scale on top with a remaining unaffected coating beneath. For Ti-Si-$B_{2\pm z}$ this steady state region is accessed at around 34 at.% Si, whereas already 18 at.% Si are sufficient for Hf-Si-$B_{2\pm z}$ to reach this region at around 1050 °C. Cr-Si-$B_{2\pm z}$ with 16 at.% Si suggest to be even more resistant, exhibiting a more or less unchanged mass signal throughout the whole temperature range up to 1400 °C.

To further evaluate and understand these trends in mass gain,

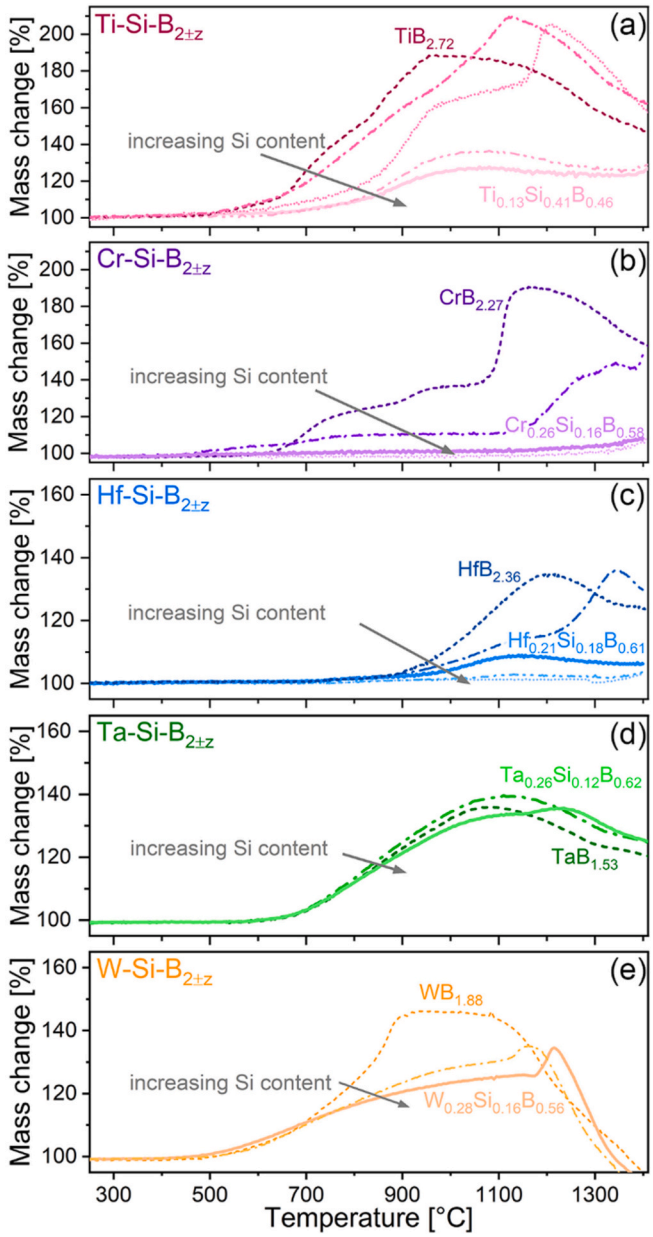

Fig. 2. Mass change during dynamic oxidation performed in a TG system using synthetic air and a heating rate of 10 K/min. Dashed lines represent the binary coatings, $TiB_{2.72}$ (a), $CrB_{2.27}$ (b), $HfB_{2.36}$ (c), $TaB_{1.53}$ (d) and $WB_{1.88}$ (e). Dashed-dot and dotted lines represent TM-Si-$B_{2\pm z}$ coatings with various Si contents. Solid lines represent the TM-Si-$B_{2\pm z}$ coatings which were investigated in more detail, $Ti_{0.13}Si_{0.41}B_{0.46}$ (a), $Cr_{0.26}Si_{0.16}B_{0.58}$ (b), $Hf_{0.21}Si_{0.18}B_{0.61}$ (c), $Ta_{0.26}Si_{0.12}B_{0.62}$ (d), and $W_{0.28}Si_{0.16}B_{0.56}$ (e).

measured during dynamic oxidation, isothermal oxidation treatments at two temperatures, 900 °C and 1100 °C, have been conducted for selected coatings. We aimed for 1 h oxidation time, but due to the high oxidation rate the time was shorter for some coatings, see Fig. 3. At 900 °C isothermal oxidation results in a mass increase following a parabolic rate law for $Ta_{0.26}Si_{0.12}B_{0.62}$, $Ti_{0.13}Si_{0.41}B_{0.46}$, and $Hf_{0.21}Si_{0.18}B_{0.61}$, see Fig. 3a respectively. In contrast, $W_{0.28}Si_{0.16}B_{0.56}$ exhibits a paralinear behavior, having a strong linear region during the initial oxidation process – see also inset in Fig. 3a. As already suggested by the results presented in Fig. 2b, $Cr_{0.26}Si_{0.16}B_{0.58}$ exhibits a mass gain being below the resolution limit of the TG system, hence a strongly retarded growth kinetic. Oxidizing the coating materials at 1100 °C – being located in the steady state region observed for $Ti_{0.13}Si_{0.41}B_{0.46}$ and $Hf_{0.21}Si_{0.18}B_{0.61}$,

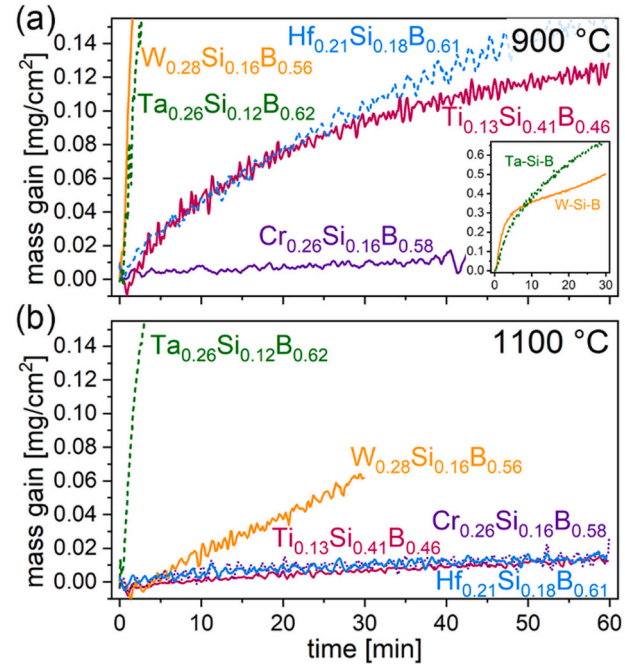

Fig. 3. Mass gain during isothermal oxidation at 900 °C (a), and 1100 °C (b). The inset in (a) shows the full mass gain for $Ta_{0.26}Si_{0.12}B_{0.62}$, and $W_{0.28}Si_{0.16}B_{0.56}$ at 900 °C.

seen in Fig. 2 – interesting effects occur compared to 900 °C. For the selected $Ti_{0.13}Si_{0.41}B_{0.46}$, $Hf_{0.21}Si_{0.18}B_{0.61}$ and $Cr_{0.26}Si_{0.16}B_{0.58}$ coatings, the mass increase is very low (again in the range of the resolution limit of the TG system), hence suggesting a very low oxide growth rate (visual inspection indicate well adherent and dense oxide scales). Due to the resolution limit of the TG system no precise parabolic rate constants (k_p) were determined. However they are at least below $1 \cdot 10^{-11}$ kg^2m^{-4} s^{-1}, when compared to k_p values and TG data of $HfN_{1.5}$ oxidized under the same conditions at 740 °C in Ref. [24]. $Ta_{0.26}Si_{0.12}B_{0.62}$ on the other hand shows still a very rapid mass gain and the isothermal oxidation was stopped after 4 min due to the huge mass increase. For $W_{0.28}Si_{0.16}B_{0.56}$ the mass increases linearly, but with a total mass gain that is significantly smaller compared to 900 °C. Here, we have to mention that $W_{0.28}Si_{0.16}B_{0.56}$ appeared fully oxidized at the substrate rim (~0.7 mm wide) after oxidation at 1100 °C. Hence, the measured mass gain is an overlap of the apparently different oxidation speeds at the substrate edge and center.

To further understand the dependence of the oxide scale formation with respect to the temperature, comparative structural analysis by XRD have been conducted in the as deposited and oxidized states (isothermal treatments at 900 and 1100 °C), see Fig. 4. All binary TM-$B_{2\pm z}$ coatings crystallize in the AlB_2 prototype (SG 191), shown as colored dashed lines in the top patterns of each plot. The TM-Si-$B_{2\pm z}$ coatings are plotted as solid black lines, from top to bottom in the as deposited state as well as oxidized at 900 and 1100 °C, respectively. With the addition of Si, the predominant peaks get gradually broadened – for all systems except Ta-Si-$B_{2\pm z}$ – which eventually lead to a complete amorphization for $Ti_{0.13}Si_{0.41}B_{0.46}$ and $W_{0.28}Si_{0.16}B_{0.56}$, see Fig. 4a and e. In addition, for $Cr_{0.26}Si_{0.16}B_{0.58}$ a clear peak shift to higher 2 theta diffraction angle is visible (Fig. 4b). However, no additional Si rich phase is observed suggesting Si present as a solid solution within the diboride lattice or as an amorphous tissue phase at the grain boundaries. This fact clearly differentiates TM-Si-$B_{2\pm z}$ coatings from the well-known Si alloyed bulk ceramics where Si is present as a separate phase e.g. SiC. After isothermal oxidation at 900 °C for 60 min, $Ti_{0.13}Si_{0.41}B_{0.46}$ exhibits rutile-TiO_2 peaks along with TiB_2 and elemental Si – diamond like structure (SG 227). This suggests, that the oxide scale contains rutile-

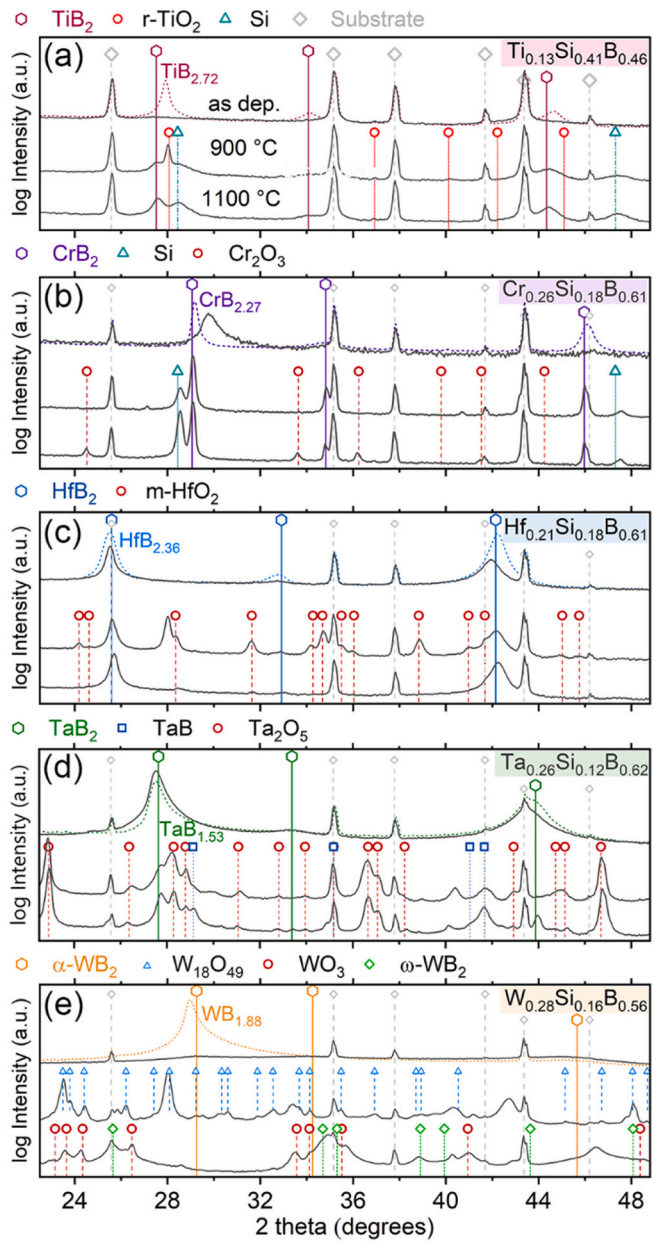

Fig. 4. XRD analysis of $Ti_{0.13}Si_{0.41}B_{0.46}$ (a), $Cr_{0.26}Si_{0.16}B_{0.58}$ (b), $Hf_{0.21}Si_{0.18}B_{0.61}$ (c), $Ta_{0.26}Si_{0.12}B_{0.62}$ (d), $W_{0.28}Si_{0.16}B_{0.56}$ (e). The upper pattern represents the as deposited state the middle after isothermal oxidation at 900 °C and the bottom one after oxidation at 1100 °C for each system. In addition to that the colored dashed line in the as deposited state represents the diffractogram of the binary coating. The solid reference lines with the colored hexagons on top represent the AlB_2 prototype structure for each diboride (TiB_2 [51], CrB_2 [52], HfB_2 [53], TaB_2 [54] and WB_2 [55]). Grey dashed lines mark the peaks resulting from the Al_2O_3 substrate [56]. Other reference lines correspond to r-TiO_2 [57],Si [58], Cr_2O_3 [59], m-HfO_2 [60], TaBle [61], Ta_2O_5 [62], $W_{18}O_{49}$ [63], WO_3 [64], ω-WB_2 [65].

TiO_2, and the remaining coating recrystallized from an X-ray amorphous structure in the as deposited state to a mixture of TiB_2 and Si grains. After oxidation at 1100 °C again TiB_2 and Si peaks are clearly indexable, but only very minor intensity for the rutile-TiO_2 – see peak at around 37°. For $Cr_{0.26}Si_{0.16}B_{0.58}$ the oxidation at 900 and 1100 °C also lead to a phase separation of elemental Si, indicated by the free standing peaks – see Fig. 4b. Furthermore, the CrB_2 peaks are shifted back to their reference position also exhibiting a decreased FWHM indicating recrystallisation. In contrast to $Ti_{0.13}Si_{0.41}B_{0.46}$ a crystalline metal oxide phase (Cr_2O_3) is only present at 1100 °C. For $Hf_{0.21}Si_{0.18}B_{0.61}$ the structural analysis in the oxidized states do not suggest any decomposition or recrystallisation processes. But, similar to the $Ti_{0.13}Si_{0.41}B_{0.46}$, strong monoclinic-$HfO_2$ peaks are visible at 900 °C, whereas at 1100 °C they are almost gone. For $Ta_{0.26}Si_{0.12}B_{0.62}$, the results of the structure analysis in the oxidized states are very similar for both temperatures with an oxide scale containing Ta_2O_5 and the remaining coating consisting of TaB_2 with small amounts of orthorhombic-TaB (SG 63). $W_{0.28}Si_{0.16}B_{0.56}$ oxidized at 900 °C exhibits a rather complex pattern, containing $W_{18}O_{49}$ as the main oxide phase. At 1100 °C ω-structured WB_2 (SG 194) is predominant, accompanied by WO_3. Hence, the amorphous coating in the as deposited state transforms into the more stable ω-WB_2 structure type [43], besides the progressing oxidation.

To gain a further insight on the formed oxide scales, SEM cross sections of all isothermally oxidized coatings are presented in Fig. 5 – $Ti_{0.13}Si_{0.41}B_{0.46}$ (a), $Cr_{0.26}Si_{0.16}B_{0.58}$ (b), $Hf_{0.21}Si_{0.18}B_{0.61}$ (c), $Ta_{0.26}Si_{0.12}B_{0.62}$ (d), and $W_{0.28}Si_{0.16}B_{0.56}$ (e), respectively. All left-hand micrographs denote the coatings oxidized at 900 °C, whereas the right-hand cross sections are oxidized at 1100 °C (respective durations see Fig. 3). For comparison in the middle part the as deposited cross sections are presented (unlike the oxidized coatings deposited on Si substrates). The dashed lines highlight the interfaces between the substrate and coating, whereby the dotted lines indicate the interfaces between the scale and coating, or between the different types of oxide scales. For all coatings, a remaining unoxidized region can be identified – please see areas between dashed and dotted lines in Fig. 5. Basically, we can distinguish between two different oxide scale formation routes: (i) one for Ti, Hf, Ta, and W based coating materials, and (ii) another one for Cr-Si-$B_{2\pm z}$. $Ti_{0.13}Si_{0.41}B_{0.46}$, $Hf_{0.21}Si_{0.18}B_{0.61}$, $Ta_{0.26}Si_{0.12}B_{0.62}$, and $W_{0.28}Si_{0.16}B_{0.56}$ exhibit an feature-less scale on top followed by a grainy oxide beneath, and a remaining unoxidized region – see Fig. 5a, c, d, and e at 900 °C. For $Ta_{0.26}Si_{0.12}B_{0.62}$ a similar morphology is also obtained at 1100 °C. Within the grainy oxide scale distinct differences occur, as a continuous layer is formed for $Hf_{0.21}Si_{0.18}B_{0.61}$ (~200 nm thick, see Fig. 5c at 900 °C) and $Ta_{0.26}Si_{0.12}B_{0.62}$ (~2 μm thick, see Fig. 5d at 900 °C), whereas for $Ti_{0.13}Si_{0.41}B_{0.46}$ and for $W_{0.28}Si_{0.16}B_{0.56}$ more globular (isolated) grains grow into the feature-less scale above, see Fig. 5a and e at 900 °C. Furthermore, the feature-less scale on top exhibits a large variation in thickness especially for $Hf_{0.21}Si_{0.18}B_{0.61}$ and $W_{0.28}Si_{0.16}B_{0.56}$ (both 900 °C). This oxide scale formation route is attributed to the low temperature regime (see also Introduction [20]) typically exhibiting a layered scale consisting of a metal oxide and boron rich oxide on top. At 1100 °C a second regime is achieved for $Ti_{0.13}Si_{0.41}B_{0.46}$, $Hf_{0.21}Si_{0.18}B_{0.61}$ and $W_{0.28}Si_{0.16}B_{0.56}$, characterized by a thin dense and continuous oxide scale. For $Ti_{0.13}Si_{0.41}B_{0.46}$ and $Hf_{0.21}Si_{0.18}B_{0.61}$ a scale thickness of only 100 to 150 nm is reached after isothermal oxidation at 1100 °C for 60 min. When comparing the morphology with the structural results (see Fig. 4), it is obvious that the crystalline oxide phase is always metal-based at the remaining coating to scale interface, whereas the feature less layer is supposed to be amorphous and B or Si dominated and hence not visible within the X-ray diffractogram. Furthermore, following the low temperature regime, the oxide scale causes higher mass gain during isothermal oxidation compared to minor mass increase for the thin dense feature-less layers at higher temperatures – compare Figs. 3 and 5. Based on the thermo gravimetry measurements, $Cr_{0.26}Si_{0.16}B_{0.58}$ exhibits a low oxide growth rate at both temperatures. However, the recrystallisation effects superimpose with the oxidation process, and therefore no clear separation between the very thin scale and coating is possible within Fig. 5b – hence, further details by TEM will be presented in Fig. 7.

Considering the influence of water vapor on the B_2O_3 growth – causing the formation of volatile boron acid – the experimental set-up used suppresses this effect. Due to the evacuation and flushing with He of the TG-furnace prior to each measurement and the use of synthetic air the amount of water vapor is significantly low compared to a conventional furnace. This leads to the fact, that a distinct boron oxide

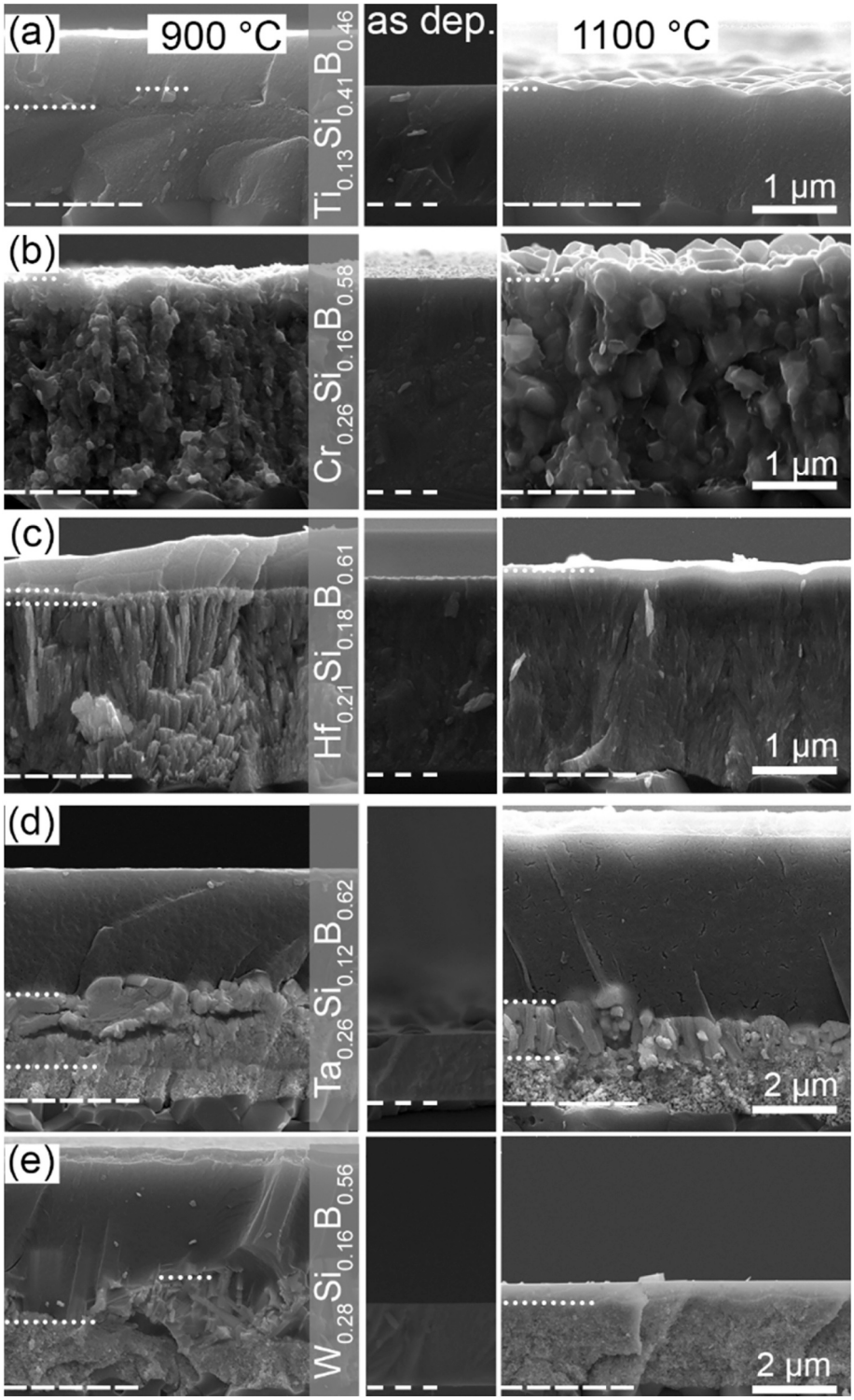

Fig. 5. SEM fracture cross section of $Ti_{0.13}Si_{0.41}B_{0.46}$ (a), $Cr_{0.26}Si_{0.16}B_{0.58}$ (b), $Hf_{0.21}Si_{0.18}B_{0.61}$ (c), $Ta_{0.26}Si_{0.12}B_{0.62}$ (d), and $W_{0.28}Si_{0.16}B_{0.56}$ (e) after isothermal oxidation at 900 °C (left side) and 1100 °C (right side). For comparison the as deposited state is shown in the middle. White dashed lines represent the different interfaces.

formation is easier visible within the used TG-setup.

Hence, additional isothermal oxidation treatments have been conducted on sapphire substrates in a conventional furnace in ambient air to also consider the effect of water vapor. Furthermore, based on the excellent oxidation resistance obtained within the TG-system, we oxidized selected samples even at higher temperatures and longer durations. We selected the Hf-Si-$B_{2\pm z}$ and Cr-Si-$B_{2\pm z}$ system for this analysis to compare one sample of each scale formation route. Furthermore, Hf-Si-$B_{2\pm z}$ was chosen as it exhibits good protectability already at lower Si contents and the binary coating (HfB_2) was also more familiar to us from a previous study [24]. However, those two samples are not substitutionary for the other systems, but should highlight the potential oxidation resistance using the described approach of Si alloyed TM-diborides.

Fig. 6 shows TEM analysis of $Hf_{0.21}Si_{0.18}B_{0.61}$ oxidized on a sapphire substrate at 1200 °C for 3 h. The bright field image (BF) clearly indicate the remaining coating from bottom to top, followed by a bright but very thin oxide scale on top. The as deposited coating thickness decreased by 100 nm from 2.4 to 2.3 μm after oxidation, whereas the oxide scale itself obtains a thickness of 400 nm. The oxide scale appears amorphous in the selected area electron diffraction (SAED) analysis, see Figure 6c_I, compared to a nicely defined AlB_2 prototype based HfB_2 (see Figure 6c_{II}) with a decreasing column size from top to bottom. The EDX line scan shows a very sharp interface towards the sapphire substrate and an equal distribution of Hf, B and Si over the whole remaining coating thickness. Furthermore, the line scan suggests a boron enrichment at the coating oxide interface as well as an oxide scale dominated by silicon with some additions of boron. However, the accuracy of EDX to quantify boron is very low, hence the obtained compositions have to be interpreted with care. Si and Hf also overlap within the EDX spectra causing an additional overestimation of Hf on the cost of Si. Additional EELS analysis suggests that the boron content in the oxide scale is significantly lower than evaluated by EDX. The chemical composition of the oxide scale on top of $Hf_{0.21}Si_{0.18}B_{0.61}$ determined with EELS is about $Si_{0.46}B_{0.03}O_{0.51}$.

In contrast, $Cr_{0.26}Si_{0.16}B_{0.58}$ oxidized at 1200 °C for 3 h has a rather different appearance during TEM analysis (Fig. 7). First of all, the high-angle annular dark-field (HAADF, see Fig. 7a) as well as the bright field image (see Fig. 7b) show, that the remaining coating is completely recrystallized exhibiting large globular grains with some voids in-between. Furthermore, the HAADF image exhibits bright and dark appearing grains representing regions with higher atomic number (bright) and lower atomic number (dark). Along with the EDX line-scan (Fig. 7c) Cr-rich and Si-rich grains can be identified. In addition, further XRD analysis clearly prove CrB_2 next to elemental Si peaks similar to the results presented in Fig. 4. Hence, bright areas represent CrB_2 whereas darker areas are Si enriched grains. Furthermore, Cr and O overlap within the EDX spectra, causing the overestimation of O in CrB_2. Nevertheless, on top of the decomposed microstructure also a very thin and dense oxide scale can be found. EDX maps (corresponding STEM and BF image in Fig. 7d and e with the respective elemental maps for Cr, O, B, and Si, respectively) nicely depict, that the oxide scale consists of two layers with Cr_2O_3 crystals on the outside and silica on the coating to oxide scale interface – see bright orange area in the Si map. Due to the recrystallized remaining coating the surface is rather rough and the oxide scale thickness varies between 180 and 750 nm exhibiting an average thickness of 400 ± 137 nm. The remaining coating thickness was close to the original thickness of about 2.6 μm, but exhibiting a much higher standard deviation due to the roughness.

4. Discussion

The results clearly prove the positive effects of silicon when alloyed to TM boride based coatings for enhancing the oxidation resistance. Within the investigated TM-Si-$B_{2\pm z}$ coating materials (TM = Ti, Cr, Hf, Ta, and W), two different oxidation routes can be distinguished: *(i)* one for Si alloyed Ti, Hf, Ta, and W based thin films, *(ii)* and another one for Cr-Si-$B_{2\pm z}$.

For $Ti_{0.13}Si_{0.41}B_{0.46}$, $Hf_{0.21}Si_{0.18}B_{0.61}$, $Ta_{0.26}Si_{0.12}B_{0.62}$, and $W_{0.28}Si_{0.16}B_{0.56}$ the addition of Si flattens the slope of the mass gain during dynamic oxidation, leading to decreased parabolic rate constants at 900 °C compared to their binary counterparts. Compared to the growth of the binary $HB_{2.3}$ coating at 900 °C shown in [24] the k_p value is reduced from $1.4 \cdot 10^{-9}$ to $7.4 \cdot 10^{-10}$ $kg^2m^{-4}s^{-1}$. Furthermore, TaB_{2-z} is reported to exhibit linear growth kinetics at 700 °C [18] (confirmed also with isothermal TG measurement of $TaB_{1.5}$ in this work), which changes to a parabolic growth through the addition of silicon. The SEM cross-sections after oxidation at 900 °C (Fig. 5) suggest, that the decreased k_p is due to a "densification" of the outer boron oxide layer through the addition of Si. Furthermore, in case of Ta—B the B-Si-O scale fills up cracks within the Ta_2O_5 layer, causing most probably the transition from a linear to a parabolic growth. In general, for these 4 systems the oxide scale morphology at 900 °C is in good agreement with the so-called low temperature regime [20], obtaining an amorphous boron rich oxide on top and crystalline metal oxide beneath. Nevertheless, the addition of Si increases the oxidation resistance also at 900 °C, but the growth rates are still too high to enable long time protection. The total mass of the 2.31 μm thick $Hf_{0.21}Si_{0.18}B_{0.61}$ was 2 mg/cm^2 hence the approximate time till the coating is fully oxidized would be around 24 h (being still relatively good considering a 2.31 μm thin coating). However, the situation is even better above 1100 °C. At these temperatures a very protective, amorphous Si rich oxide scale is formed on top. In contrast to the scale formed at 900 °C the formation of a crystalline metal oxide is mainly suppressed. This scale enables oxide growth rates being below the mass resolution of the TG system at 1100 °C, resulting in

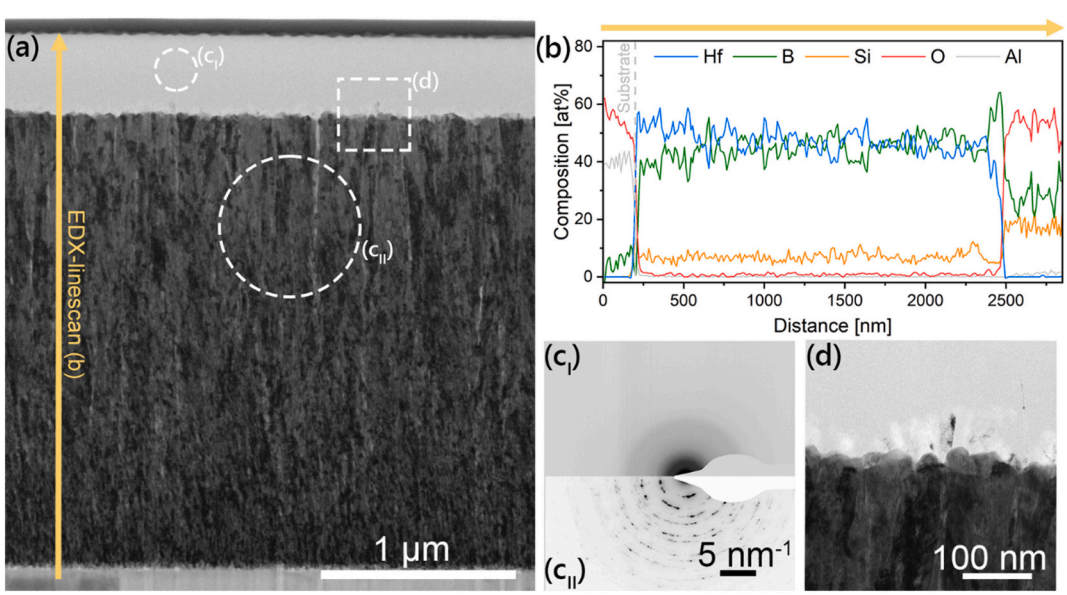

Fig. 6. TEM investigation of $Hf_{0.21}Si_{0.18}B_{0.61}$ oxidized in ambient air at 1200 °C for 3 h. (a) BF image covering the whole coating and the formed oxide scale on top. (b) EDX line scan over the whole thickness as indicated by the arrow in (a). (c) SAED image of the oxide scale and (d) magnified interface between the remaining coating and the oxide scale. Additional EELS analysis of the coating/scale interface is provided as Supplementary material.

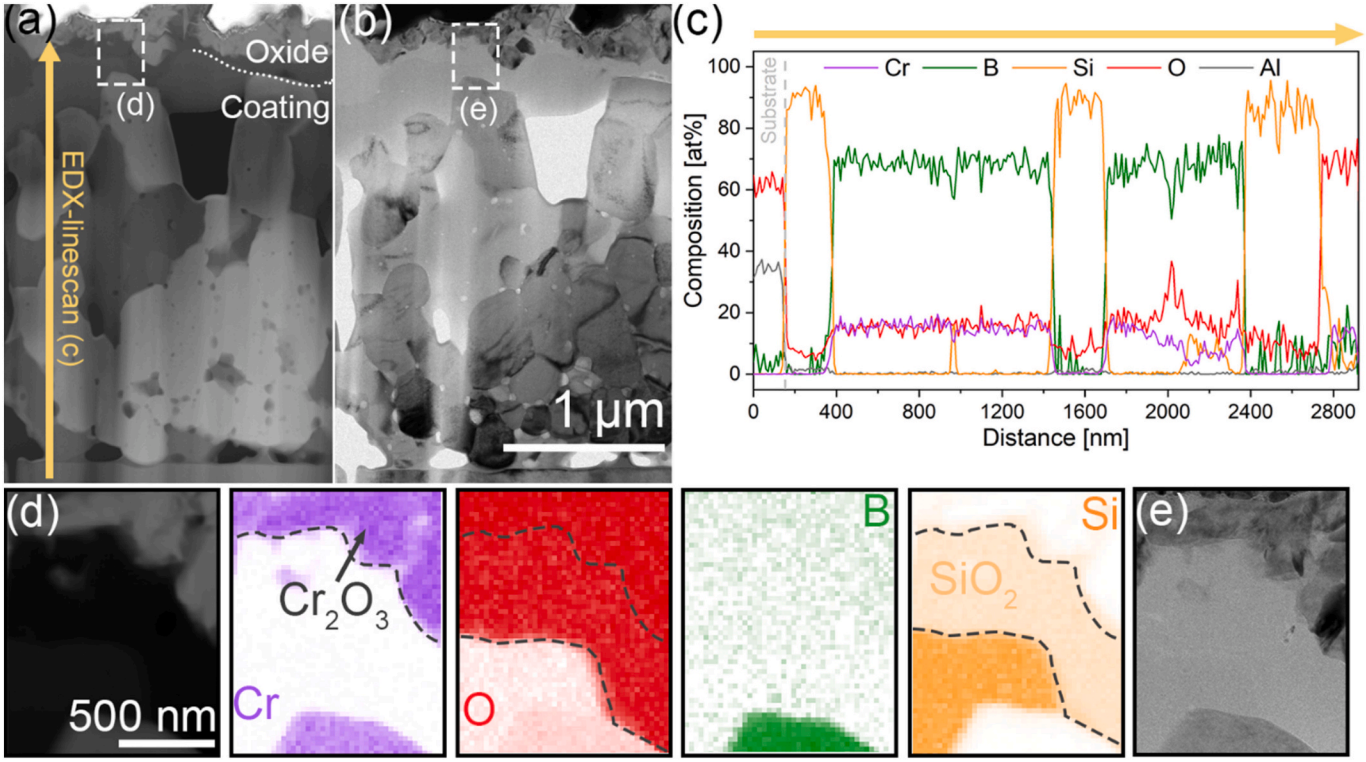

Fig. 7. $Cr_{0.26}Si_{0.16}B_{0.58}$ oxidized in ambient air at 1200 °C for 3 h. High angle annular dark field (HAADF) image (a) and BF image (b) of the whole remaining coating including the substrate on bottom and oxide scale on top. (c) EDX linescan over the whole coating thickness as indicated by the arrow in (a). STEM image and elemental EDX maps (d) of the area indicated by dashed lines in (a) and (b) and corresponding BF image (e).

an oxide scale thickness of only ~100 nm after 1 h at 1100 °C in synthetic air for e.g. $Ti_{0.13}Si_{0.41}B_{0.46}$ and $Hf_{0.21}Si_{0.18}B_{0.61}$. Even at 1200 °C for 3 h in ambient air the $Hf_{0.21}Si_{0.18}B_{0.61}$ as deposited coating thickness decreased only by 100 nm exhibiting a 400 nm thick oxide scale. This is even lower as observed for MAX or MAB phases being suggested as promising oxidation resistant materials [36]. Furthermore, the oxide growth rates are definitely lower compared to sprayed MCrAlY coatings currently used as bond coats for turbine blade protection in jet engines [44]. This highlights the large potential of these coating materials, especially Hf-Si-$B_{2\pm z}$ and Ti-Si-$B_{2\pm z}$. An interesting peculiarity of these diboride based coatings is, that at high temperatures a strongly Si enriched oxide layer is formed, whereby in contrast for e.g. Ti-Si-N the silicon oxide is located between the TiO_2 grains [45].

Comparing these results with bulk ceramics, the temperature depended scale formation is also reported for ZrB_2 and HfB_2 bulks, where Si is added as SiC or as a metal silicide during sintering. Below ~1100 °C the oxidation behavior is very similar to pure diboride ceramics exhibiting a layered oxide scale with B_2O_3 on top and the metal oxide e.g. ZrO_2 below (SiC is left mainly unoxidized) [46]. This is related to the fact that ZrB_2 oxidizes faster than SiC in this temperature regime. Above 1100 °C the formation of an outer SiO_2 rich layer and an inner ZrO_2 layer is reported. SiC starts to oxidize and due to the B_2O_3 evaporation, which becomes significant at these temperatures, the surface layer only contains a small amount of B_2O_3 [46]. The reported evaporation of B_2O_3 is also clearly visible as mass loss during dynamic oxidation of the binary coatings, see Fig. 2. For our data set, this mechanism coincidences with the formation of the steady mass gain plateau. Hence, if boron oxide immediately evaporates from the surface above ~1100 °C the more protective Si rich scale can step in. However, the coating has to contain a certain amount of Si to enable the formation of a dense Si enriched scale. The required amount of Si of course varies for the different TM-Si-$B_{2\pm z}$ coatings. Whereas, for Hf-Si-$B_{2\pm z}$ the plateau forms already at a Si content of 18 at.%, 34 at.% are needed for the Ti-Si-$B_{2\pm z}$ coatings in this study.

From a thermodynamic point of view the metals can be divided into two groups: metal oxides with a standard Gibbs free energy of formation (kJ•mol^{-1} O_2 at 298.15 K) lower (HfO_2, TiO_2) or higher (Ta_2O_5, Cr_2O_3, WO_3) than SiO_2 [47]. Hence, the driving force to form the metal oxide is highest for HfO_2 and SiO_2 should be formed easiest when competing with tungsten. This however does not reflect the experimental observations. Therefore, we suggest kinetic reasons (e.g. diffusion of Si within the boride based coatings) being predominant. A further important factor is the influence of Si on phase formation in these TM-Si-$B_{2\pm z}$ based coating materials. In relation to the specific kinetics prevailing during PVD, we could not observe any phase separation of Si based phases within all TM-Si-$B_{2\pm z}$ investigated in the as deposited state. However, during progressing oxidation, phase separation processes lead to the formation of Si rich domains (e.g. Cr-Si-$B_{2\pm z}$), supporting the diffusion driven formation of Si enriched oxide scale.

The second oxidation route is achieved for Cr-Si-$B_{2\pm z}$ based coatings, exhibiting a distinctively different oxide scale formation. TEM investigation of $Cr_{0.26}Si_{0.16}B_{0.58}$ oxidized at 1200 °C revealed, that the oxide scale does not consist of a single Si rich oxide layer, but of two layers with crystalline Cr_2O_3 on top and amorphous Si—O below. Hence, unlike to the other TM-Si-$B_{2\pm z}$ coatings investigated in this study, the metal oxide is not located at the coating to oxide scale interface but on the top. This could be due to the fact, that in contrast to the other TM-oxides investigated, Cr ions primarily diffuse outwards in Cr_2O_3 [48]. Hence, the oxide grows outwards at the scale to surface interface (via cation outward diffusion) and not at the scale to coating interface, as for TiO_2. This could further cause that $Cr_{0.26}Si_{0.16}B_{0.58}$ exhibits a low growth rate already at temperatures below 1000–1100 °C. However, the origin of the different behavior of Cr-Si-$B_{2\pm z}$ could be also influenced by the stepwise oxidation process of the binary system. In Ref. [49] the formation of a chromium borate is reported instead of separate metal and boron oxide as for e.g. HfB_2. Overall $Cr_{0.26}Si_{0.16}B_{0.58}$ stands out due to its continuous low oxide growth rate from room temperature up to 1400 °C forming a highly protective and dense scaling. Compared to Cr—Si based

alloys [50] the oxide growth rates of the $Cr_{0.26}Si_{0.16}B_{0.58}$ coating is even lower.

Dynamic oxidation analysis of amorphous Ti-B-Si coatings at 900 °C, done by Grancic et al. [33], suggest a comparable mass gain already at lower total Si contents in the thin films compared to this study (binary Ti—B coatings are in good agreement). This is a strong indication for an influence of the morphology and the B/Me ratio. Further comparison with studies in literature shows, that dynamic oxidation of TaB_2 as well as TaB_2 + 20 wt% SiC powders is very similar to what is observed in this study. A study on $Zr_{0.27}Si_{0.08}B_{0.65}$ coatings, suggests that after oxidized at 1200 °C 1 h a 2.5 μm thick oxide scale mostly consisting of SiO_2 with inclusions of ZrO_2 [34]. Along with studies on bulk ZrB_2 based ceramics this suggests that the scale formation of Zr-B + Si is similar to Hf-B + Si. In summary, comparing the here obtained results for various TM-Si-$B_{2\pm z}$ coatings (TM = Ti, Cr, Hf, Ta, and W) with other systems investigated in literature, similar oxide scale formation processes can be identified. However, the oxide scale growth rates observed in this study ($k_p < 10^{-11}$ kg^2m^{-4} s^{-1}, 1100 °C) are significantly lower as reported for e.g. TMB_2/SiC bulk ceramics (k_p 10^{-8}–10^{-6} kg^2m^{-4} s^{-1}, above 1100 °C [12]). This might be caused by the fact that TM-Si-$B_{2\pm z}$ coatings are single phased structured, whereas Si is present as a separate phase in TMB_2/SiC bulk ceramics. Furthermore, in contrast to bulk ceramics no crystalline TM-oxide is formed above 1100 °C for TM-Si-$B_{2\pm z}$ coatings.

5. Conclusion

Physical vapor deposited TM-Si-$B_{2\pm z}$ (TM = Ti, Cr, Hf, Ta, W) based coating materials were successfully proven to exhibit drastically enhanced oxidation resistance compared to their binary counterparts. In detail, $Hf_{0.21}Si_{0.18}B_{0.61}$ and $Cr_{0.26}Si_{0.16}B_{0.58}$ thin films (both around 2.4 μm thick) reveal strongly retarded oxidation kinetics leading to only 400 nm oxide scale thickness after 3 h oxidation in ambient air at 1200 °C. For these coating materials, oxide scale growth rates (k_p) smaller than 10^{-11} kg^2m^{-4} s^{-1} at 1100 °C have been achieved, being three orders of magnitude lower compared to TMB_2/SiC bulk ceramics. In contrast to well-described Si containing bulk ceramics, the investigated TM-Si-$B_{2\pm z}$ coatings appear single phase structured without any Si separation visible during structural analysis in the as deposited state.

In general, for Ti-Si-$B_{2\pm z}$, Hf-Si-$B_{2\pm z}$ and W-Si-$B_{2\pm z}$ coatings a temperature depended oxide scale formation process has been identified. At 900 °C these coatings form layered oxide scales consisting of a crystalline metal oxide (at the interface to the unaffected coating material) with an amorphous boria rich scale on top. During dynamic oxidation, Si promotes the evolution of a steady state region at around 1000 to 1100 °C (plateau within the TG mass signal), with a flattened mass increase ahead. The formation of this steady state region requires different amounts of Si, e.g. 34 at.% for Ti-Si-$B_{2\pm z}$ compared to 18 at.% for Hf-Si-$B_{2\pm z}$. Above 1100 °C, highly protective, glassy like Si rich oxide scales are predominant (i.e. Hf-Si-$B_{2\pm z}$ only 100 nm after 1 h). W-Si-B $B_{2\pm z}$ also showed a strongly retarded oxide growth at 1100 °C, however being higher compared to Ti-Si-$B_{2\pm z}$ and Hf-Si-$B_{2\pm z}$. For Ta-Si-$B_{2\pm z}$ the Si contents (up to 12 at. %) investigated in this study were either not sufficient to form the more protective scale above 1100 °C, or Ta-Si-$B_{2\pm z}$ coatings exhibit a different scale formation mechanism, which does not favor the Si rich oxide scale. Furthermore, Cr-Si-$B_{2\pm z}$ coatings show a different behavior with already low oxide growth rates ($< 10^{-11}$ kg^2m^{-4} s^{-1}) below 1000 °C, but also strongly retarded oxidation kinetics up to 1200 °C. In comparison to Hf-Si-$B_{2\pm z}$ only 16 at.% Si are required to access this behavior. The oxide scale is based on an amorphous Si rich domain with a thin Cr_2O_3 layer on top.

In summary, this study highlights the enormous potential of single phased structured TM-Si-$B_{2\pm z}$ coatings for oxidation protection at extremely high temperatures.

Supplementary data to this article can be found online at https://doi.org/10.1016/j.surfcoat.2022.128178.

CRediT authorship contribution statement

T. Glechner: Conceptualization, Investigation, Writing – original draft. **H.G. Oemer:** Investigation. **T. Wojcik:** Investigation. **M. Weiss:** Investigation. **A. Limbeck:** Resources. **J. Ramm:** Resources, Writing – review & editing. **P. Polcik:** Resources, Writing – review & editing. **H. Riedl:** Supervision, Writing – review & editing.

Declaration of competing interest

The authors declare that they have no known competing financial interests or personal relationships that could have appeared to influence the work reported in this paper.

Acknowledgment

The financial support by the Austrian Federal Ministry for Digital and Economic Affairs, the National Foundation for Research, Technology and Development and the Christian Doppler Research Association is gratefully acknowledged (Christian Doppler Laboratory "Surface Engineering of high-performance Components"). We also thank for the financial support of Plansee SE, Plansee Composite Materials GmbH, and Oerlikon Balzers, Oerlikon Surface Solutions AG. In addition, we want to thank the X-ray center (XRC) of TU Wien for beam time as well as the electron microscopy center - USTEM TU Wien - for using the SEM and TEM facilities. The authors acknowledge TU Wien Bibliothek for financial support through its Open Access Funding Programme.

Appendix A. Appendix

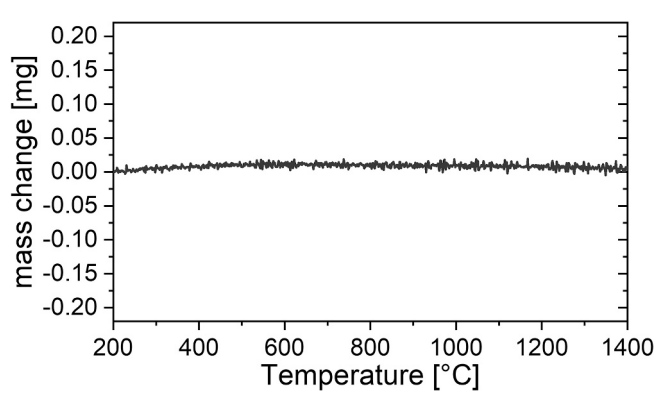

Fig. A1. Mass change of a bare (uncoated) Al_2O_3 substrate during dynamic oxidation performed in a TG-system using synthetic air and a heating rate of 10 K/min (in correspondence to Fig. 2).

References

[1] W.G. Fahrenholtz, G.E. Hilmas, Ultra-high temperature ceramics: materials for extreme environments, Scr. Mater. 129 (2017) 94–99.
[2] E. Sani, L. Mercatelli, M. Meucci, L. Zoli, D. Sciti, Lanthanum hexaboride for solar energy applications, Sci. Rep. 7 (2017) 718.
[3] E. Sani, M. Meucci, L. Mercatelli, A. Balbo, C. Musa, R. Licheri, R. Orrù, G. Cao, Titanium diboride ceramics for solar thermal absorbers, Sol. Energy Mater. Sol. Cells 169 (2017) 313–319.
[4] C. Subramanian, A.K. Suri, T. Murthy, Development of boron-based materials for nuclear applications, BARC Newsl. 313 (2010) 14.
[5] P.H. Mayrhofer, C. Mitterer, J.G. Wen, J.E. Greene, I. Petrov, Self-organized nanocolumnar structure in superhard TiB2 thin films, Appl. Phys. Lett. 86 (2005), 131909.
[6] H.-Y. Chung, M.B. Weinberger, J.B. Levine, R.W. Cumberland, A. Kavner, J.-M. Yang, S.H. Tolbert, R.B. Kaner, Synthesis of ultra-incompressible superhard rhenium diboride at ambient pressure, Science 316 (2007) 436–439.
[7] Q. Gu, G. Krauss, W. Steurer, Transition metal borides: superhard versus ultra-incompressible, Adv. Mater. 20 (2008) 3620–3626.
[8] Y. Song, S. Zhang, X. Wu, Oxidation and electronic-specific heat of YB2, J. Alloys Compd. 322 (2001) L14–L16.
[9] O. Hunold, M. Wiesing, T. de los Arcos, G.Grundmeier Denis, J.M. Schneider, Music, Influence of O2 exposure on the interaction between CH4 and amorphous AlYB14, Appl. Surf. Sci. 392 (2017) 1165–1172.
[10] T. Tanaka, S. Otani, Y. Ishizawa, Preparation of single crystals of YB66, J. Cryst. Growth 73 (1985) 31–36.
[11] J.W. Zimmermann, G.E. Hilmas, W.G. Fahrenholtz, R.B. Dinwiddie, W.D. Porter, H. Wang, Thermophysical properties of ZrB2and ZrB2–SiC ceramics, J. Am. Ceram. Soc. 91 (2008) 1405–1411.
[12] W.G. Fahrenholtz, G.E. Hilmas, Oxidation of ultra-high temperature transition metal diboride ceramics, Int. Mater. Rev. 57 (2012) 61–72.
[13] F. Monteverde, L. Scatteia, Resistance to thermal shock and to oxidation of metal diborides?SiC ceramics for aerospace application, J. Am. Ceram. Soc. 90 (2007) 1130–1138.
[14] B. Bakhit, J. Palisaitis, J. Thörnberg, J. Rosen, P.O.Å. Persson, L. Hultman, I. Petrov, J.E. Greene, G. Greczynski, Improving the high-temperature oxidation resistance of TiB2 thin films by alloying with Al, Acta Mater. 196 (2020) 677–689.
[15] B. Alling, H. Högberg, R. Armiento, J. Rosen, L. Hultman, A theoretical investigation of mixing thermodynamics, age-hardening potential and electronic structure of ternary M 1 1–x M 2 x B 2 alloys with AlB 2 type structure, Sci. Rep. 5 (2015) 1–7.
[16] V. Moraes, H. Riedl, C. Fuger, P. Polcik, H. Bolvardi, D. Holec, P.H. Mayrhofer, Ab initio inspired design of ternary boride thin films, Sci. Rep. 8 (2018) 9288.
[17] B. Bakhit, D.L.J. Engberg, J. Lu, J. Rosen, H. Högberg, L. Hultman, I. Petrov, J. E. Greene, G. Greczynski, Strategy for simultaneously increasing both hardness and toughness in ZrB2-rich Zr1−xTaxBy thin films, J. Vac. Sci. Technol. A 37 (2019), 031506.
[18] C. Fuger, B. Schwartz, T. Wojcik, V. Moraes, M. Weiss, A. Limbeck, C.A. Macauley, O. Hunold, P. Polcik, D. Primetzhofer, P. Felfer, P.H. Mayrhofer, H. Riedl, Influence of Ta on the oxidation resistance of WB2−z coatings, J. Alloys Compd. 864 (2021), 158121.
[19] D.S. King, W.G. Fahrenholtz, G.E. Hilmas, Silicon carbide–titanium diboride ceramic composites, J. Eur. Ceram. Soc. 33 (2013) 2943–2951.
[20] T.A. Parthasarathy, R.A. Rapp, M. Opeka, R.J. Kerans, A model for the oxidation of ZrB2, HfB2 and TiB2, Acta Mater. 55 (2007) 5999–6010.
[21] Y.-H. Koh, S.-Y. Lee, H.-E. Kim, Oxidation behavior of titanium boride at elevated temperatures, J. Am. Ceram. Soc. 84 (2001) 239–241.
[22] R. Naraparaju, K. Maniya, A. Murchie, W.G. Fahrenholtz, G.E. Hilmas, Effect of moisture on the oxidation behavior of ZrB2, J. Am. Ceram. Soc. 104 (2021) 1058–1066.
[23] Q.N. Nguyen, E.J. Opila, R.C. Robinson, Oxidation of ultrahigh temperature ceramics in water vapor, J. Electrochem. Soc. 151 (2004) B558.
[24] T. Glechner, O.E. Hudak, T. Wojcik, L. Haager, F. Bohrn, H. Hutter, O. Hunold, J. Ramm, S. Kolozsvári, E. Pitthan, D. Primetzhofer, H. Riedl, Influence of the non-metal species on the oxidation kinetics of Hf, HfN, HfC, and HfB2 coatings, Mater. Des. 211 (2021), 110136.
[25] M.M. Opeka, I.G. Talmy, J.A. Zaykoski, Oxidation-based materials selection for 2000°C + hypersonic aerosurfaces: theoretical considerations and historical experience, J. Mater. Sci. 39 (2004) 5887–5904.
[26] R. Bürgel, H.Jürgen Maier, T. Niendorf, Handbuch Hochtemperatur-Werkstofftechnik: Grundlagen, Werkstoffbeanspruchungen, Hochtemperaturlegierungen und -beschichtungen, Vieweg+Teubner, 2011.
[27] M.M. Opeka, I.G. Talmy, E.J. Wuchina, J.A. Zaykoski, S.J. Causey, Mechanical, thermal, and oxidation properties of refractory hafnium and zirconium compounds, J. Eur. Ceram. Soc. 19 (1999) 2405–2414.
[28] F. Monteverde, R.J. Grohsmeyer, A.D. Stanfield, G.E. Hilmas, W.G. Fahrenholtz, Densification behavior of ZrB2-MoSi2 ceramics: the formation and evolution of core-shell solid solution structures, J. Alloys Compd. 779 (2019) 950–961.
[29] T.A. Parthasarathy, M.G. Mendiratta, D.M. Dimiduk, Oxidation mechanisms in mo-reinforced Mo5SiB2(T2)–Mo3Si alloys, Acta Mater. 50 (2002) 1857–1868.
[30] H. Riedl, C.M. Koller, A. Limbeck, J. Kalaš, P. Polcik, P.H. Mayrhofer, Oxidation behavior and tribological properties of multilayered Ti-Al-N/Mo-Si-B thin films, J. Vac. Sci. Technol. A 33 (2015), 05E129.
[31] K. Ihara, K. Ito, K. Tanaka, M. Yamaguchi, Mechanical properties of Mo5SiB2 single crystals, Mater. Sci. Eng. A 329–331 (2002) 222–227.
[32] B.P. Bewlay, M.R. Jackson, J.-C. Zhao, P.R. Subramanian, M.G. Mendiratta, J. J. Lewandowski, Ultrahigh-temperature Nb-silicide-based composites, MRS Bull. 28 (2003) 646–653.
[33] B. Grančič, M. Mikula, T. Roch, P. Zeman, L. Satrapinskyy, M. Gregor, T. Plecenik, E. Dobročka, Z. Hájovská, M. Mičušík, A. Šatka, M. Zahoran, A. Plecenik, P. Kúš, Effect of Si addition on mechanical properties and high temperature oxidation resistance of Ti–B–Si hard coatings, Surf. Coat. Technol. 240 (2014) 48–54.
[34] F.V. Kiryukhantsev-Korneev, M.V. Lemesheva, N.V. Shvyndina, E.A. Levashov, A. Y. Potanin, Structure, mechanical properties, and oxidation resistance of ZrB2, ZrSiB, and ZrSiB/SiBC coatings, Prot. Met. Phys. Chem. Surf. 54 (2018) 1147–1156.
[35] P. Kiryukhantsev-Korneev, A. Sytchenko, Y. Pogozhev, S. Vorotilo, A. Orekhov, P. Loginov, E. Levashov, Structure and properties of Zr-Mo-Si-B-(N) hard coatings obtained by d.C. magnetron sputtering of ZrB2-MoSi2 target, Materials 14 (2021), https://doi.org/10.3390/ma14081932.
[36] J.-O. Achenbach, R. Sahu, B. Völker, M. Hans, D. Primetzhofer, D.J. Miljanovic, C. Scheu, J.M. Schneider, Synthesis and properties of orthorhombic MoAlB coatings, Coat. World 9 (2019) 510.
[37] T. Glechner, R. Hahn, L. Zauner, S. Rißlegger, A. Kirnbauer, P. Polcik, H. Riedl, Structure and mechanical properties of reactive and non-reactive sputter deposited WC based coatings, J. Alloys Compd. 885 (2021), 161129.
[38] A. Cakara, M. Bonta, H. Riedl, P.H. Mayrhofer, A. Limbeck, Development of a multi-variate calibration approach for quantitative analysis of oxidation resistant Mo–Si–B coatings using laser ablation inductively coupled plasma mass spectrometry, Spectrochim. Acta Part B At. Spectrosc. 120 (2016) 57–62.
[39] J. Neidhardt, S. Mráz, J.M. Schneider, E. Strub, W. Bohne, B. Liedke, W. Möller, C. Mitterer, Experiment and simulation of the compositional evolution of Ti–B thin films deposited by sputtering of a compound target, J. Appl. Phys. 104 (2008), 063304.
[40] B. Bakhit J. Palisaitis Z. Wu M.A. Sortica D. Primetzhofer Age hardening in superhard ZrB2-rich Zr1-xTaxBy thin films, Scr. Mater. (n.d.). https://www.sciencedirect.com/science/article/pii/S1359646220306254.
[41] J. Thörnberg, J. Palisaitis, N. Hellgren, F.F. Klimashin, N. Ghafoor, I. Zhirkov, C. Azina, J.-L. Battaglia, A. Kusiak, M.A. Sortica, J.E. Greene, L. Hultman, I. Petrov, P.O.Å. Persson, J. Rosen, Microstructure and materials properties of understoichiometric TiBx thin films grown by HiPIMS, Surf. Coat. Technol. 404 (2020), 126537.
[42] E.A. Gulbransen, K.F. Andrew, Kinetics of the oxidation of pure tungsten from 500° to 1300°C, J. Electrochem. Soc. 107 (1960) 619.
[43] V. Moraes, C. Fuger, V. Paneta, D. Primetzhofer, P. Polcik, H. Bolvardi, M. Arndt, H. Riedl, P.H. Mayrhofer, Substoichiometry and tantalum dependent thermal stability of α-structured W-Ta-B thin films, Scr. Mater. 155 (2018) 5–10.
[44] W. Brandl, H.J. Grabke, D. Toma, J. Krüger, The oxidation behaviour of sprayed MCrAlY coatings, Surf. Coat. Technol. 86–87 (1996) 41–47.
[45] Y. Moritz, C. Saringer, M. Tkadletz, A. Stark, N. Schell, I. Letofsky-Papst, C. Czettl, M. Pohler, N. Schalk, Oxidation behavior of arc evaporated TiSiN coatings investigated by in-situ synchrotron X-ray diffraction and HR-STEM, Surf. Coat. Technol. 404 (2020), 126632.
[46] A. Rezaie, W.G. Fahrenholtz, G.E. Hilmas, Evolution of structure during the oxidation of zirconium diboride–silicon carbide in air up to 1500°C, J. Eur. Ceram. Soc. 27 (2007) 2495–2501.
[47] W.M. Haynes, CRC Handbook of Chemistry and Physics, 93rd edition, CRC Press LLC, Baton Rouge, 2012.
[48] N. Birks, G.H. Meier, F.S. Pettit, Introduction to the High Temperature Oxidation of Metals, Cambridge University Press, 2006.
[49] M.L. Emiliani, Characterization and oxidation resistance of hot-pressed chromium diboride, Mater. Sci. Eng. A 172 (1993) 111–124.
[50] A.S. Ulrich, P. Pfizenmaier, A. Solimani, U. Glatzel, M.C. Galetz, Improving the oxidation resistance of Cr-Si-based alloys by ternary alloying, Corros. Sci. 165 (2020), 108376.
[51] International Center of Diffraction Data, Powder Diffraction File 04-004-7184, 2019.
[52] International Center of Diffraction Data, Powder Diffraction File 04-003-6121, 2019.
[53] International Center of Diffraction Data, Powder Diffraction File 04-002-0174, 2019.
[54] International Center of Diffraction Data, Powder Diffraction File 04-001-2977, 2019.
[55] International Center of Diffraction Data, Powder Diffraction File 04-003-6624, 2019.
[56] International Center of Diffraction Data, Powder Diffraction File 04-010-6477, 2019.
[57] International Center of Diffraction Data, Powder Diffraction File 04-002-2667, 2019.
[58] International Center of Diffraction Data, Powder Diffraction File 04-006-4528, 2019.

[59] International Center of Diffraction Data, Powder Diffraction File 04-015-7583, 2019.
[60] International Center of Diffraction Data, Powder Diffraction File 04-004-3850, 2019.
[61] International Center of Diffraction Data, Powder Diffraction File 04-001-2979, 2019.
[62] International Center of Diffraction Data, Powder Diffraction File 00-025-092, 2019.
[63] International Center of Diffraction Data, Powder Diffraction File 04-007-5585, 2019.
[64] International Center of Diffraction Data, Powder Diffraction File 04-005-4301, 2019.
[65] International Center of Diffraction Data, Powder Diffraction File 04-007-1000, 2019.